Organic Monolayers on Si(211) for Triboelectricity Generation: Etching Optimization and Relationship Between Electrochemistry and Current Output

Carlos Hurtado,[a] Xin Lyu,[a] Stuart Ferrie,[a] Anton P. Le Brun,[b] Melanie MacGregor,[c] Simone Ciampi,[a,*]

[a]School of Molecular and Life Sciences, Curtin University, Bentley, Western Australia 6102, Australia

[b]Australian Centre for Neutron Scattering, Australian Nuclear Science and Technology Organization, Lucas Heights, New South Wales 2234, Australia

[c]Flinders Institute for Nanoscale Science and Technology, Flinders University, Bedford Park, South Australia 5042, Australia

KEYWORDS. Triboelectricity, silicon, surface chemistry, organic monolayers, electrochemistry.

ABSTRACT. Triboelectric nanogenerators (TENGs) based on sliding silicon–organic monolayer–metal Schottky diodes are an emerging autonomous DC current supply technology. Herein, using conductive atomic force microscopy and electrochemical techniques, we explore the optimal etching conditions towards the preparation of DC TENGs on Si(211), a readily available, highly conductive, and underexplored silicon crystallographic cut. We report optimized conditions for the chemical etch of Si(211) surfaces with sub-nm rms roughness, explore Si(211) chemical passivation, and unveil a relationship between the electrochemical charge transfer behavior at the silicon–liquid interface and the zero-applied bias current output from the corresponding dynamic

1

silicon–organic monolayer–platinum system. The overall aim is to optimize the etching and functionalization of the relatively underexplored Si(211) facet, towards its application in out-of-equilibrium Schottky diodes as autonomous power supplies. We also propose the electrochemical behavior of surface-confined redox couples as a diagnostic tool to anticipate whether or not a given surface will perform satisfactorily when used in a TENG design.

1. Introduction

Semiconducting materials have revolutionized society and are the foundation of our digitized technologies. Silicon-based components are at the core of devices whose functions range from energy storage, energy conversion,[1] data processing and storage,[2] to sensing.[3]

Prompted by the pioneering work of Lindford and Chidsey,[4] expanding our ability to merge the complexity of the molecular world[5, 6] with the sturdiness of an inorganic silicon substrate has been a central motivation behind four decades of surface chemistry, electrochemistry, and molecular electronics research.[7,8, 9,10, 11,12] The ongoing quest of predictably tuning the performance and function of silicon-based devices has made tremendous progress. For instance, silicon–molecule–metal diodes have been realized experimentally,[13] and such hybrid constructs are now at the core of new autonomous power technologies, such as triboelectric nanogenerators (TENGs) harvesting mechanical vibrations and friction into electrical energy.[14, 15]

The operation of such hybrid organic–inorganic devices relies on a complete and correct understanding of how electrons cross the interface formed between silicon and either a metal or a liquid electrolyte contact.[13, 16] Being able to engineer the interfacial properties of silicon can therefore expand the performance of semiconductor devices,[17, 18] and specific monolayer chemistries can maximize the DC current output of out-of-equilibrium silicon diodes used as TENGs.[15]

Despite being readily available, silicon wafers of orientation other than ⟨111⟩ and ⟨100⟩ have received little attention by the surface science community. This point is of particular importance, as four years have already elapsed since the discovery by Huang and co-workers[19] of the surprisingly high electrical conductivity of Si(211). A limited number of follow-up works have since then demonstrated that for silicon its surface conductivity decreases in the order ⟨211⟩ >> ⟨100⟩ > ⟨111⟩,[20] and have also highlighted some of the practical consequences of this facet-dependent conductivity, such as the silica–silicon redox couple becoming reversible on Si(110) defects, which are ubiquitous even on a nominal and well-prepared Si(111) surface.[16]

We believe that one of the reasons still hindering a broader adoption, in both the electrochemistry and energy conversion fields (e.g., TENGs), of commercially available and highly conductive Si(211) and Si(110) wafers is the lack of suitable etching and surface chemistry modification procedures. Equally poorly documented are their electrical and electrochemical responses, that is, whether solid and liquid junctions made on these alternative silicon crystallographic cuts behave close or far from ideality.[21]

The purpose of this article is to define the optimal conditions for the preparation and functionalization of oxide-free and monolayer-modified Si(211) surfaces, an underexplored but readily available silicon crystallographic cut. We seek to expand the applicability of monolayer-modified Si(211) surfaces in miniaturized sliding Schottky diode TENGs, devices aimed at converting mechanical into electrical energy.

2. Results and Discussion

The focus of this report is on chemically modified phosphorus-doped Si(211), as n-type is the preferred choice for DC TENGs that rely on relatively soft metal contacts of large work function,

such as platinum.[15, 22, 23] The precise charge separation mechanism for this and similar DC TENGs is still unclear, but it most likely involves the formation of electron–hole pairs in response to a mechanical stimulus. These charges are then separated by the built-in electric field of the Schottky diode and/or by static electricity. It is also possible that negative charges generated on the platinum tip[24] and flexoelectricity[25] of the junction are also contributing to enhance the junction's electric field. Particular emphasis is placed on trying to unveil the presence (or absence) of a relationship between electrochemical charge transfer of the silicon–liquid interface and the zero-applied bias current output of the corresponding dynamic silicon–platinum system.

The expectation is to develop a diagnostic electrochemical test to help predicting which surface is more likely to perform well in a TENG setup. All silicon samples of this work were first etched to expose a hydrogen-terminated surface (Si–H, Figure 1a), which is reactive towards unsaturated organic molecules,[4, 26, 27] and therefore amenable to chemical passivation to limit anodic decomposition of the electrode. Chemical passivation was achieved via hydrosilylation of a symmetrical α,ω-dialkyne molecule (1,8-nonadyine, **1**, Figure 1a). This chemical reaction generates an alkyne-terminated monolayer (**S-1**, Figure 1a),[28] which can be further modified via a copper(I)-catalyzed azide−alkyne cycloaddition (CuAAC) reaction (**S-2**, Figure 1a).[29] The latter point, further derivatization of the alkyne film with a redox probe (azidomethylferrocene, **2**), is of central importance to the electrochemical experiments used to study the electrochemical heterogeneity and charge transport characteristics of the semiconductor–liquid junction.

This study involves a systematic screening of the etching conditions to generate a Si–H surface from oxide-coated commercial Si(211) wafers. The goal is to define etching conditions yielding
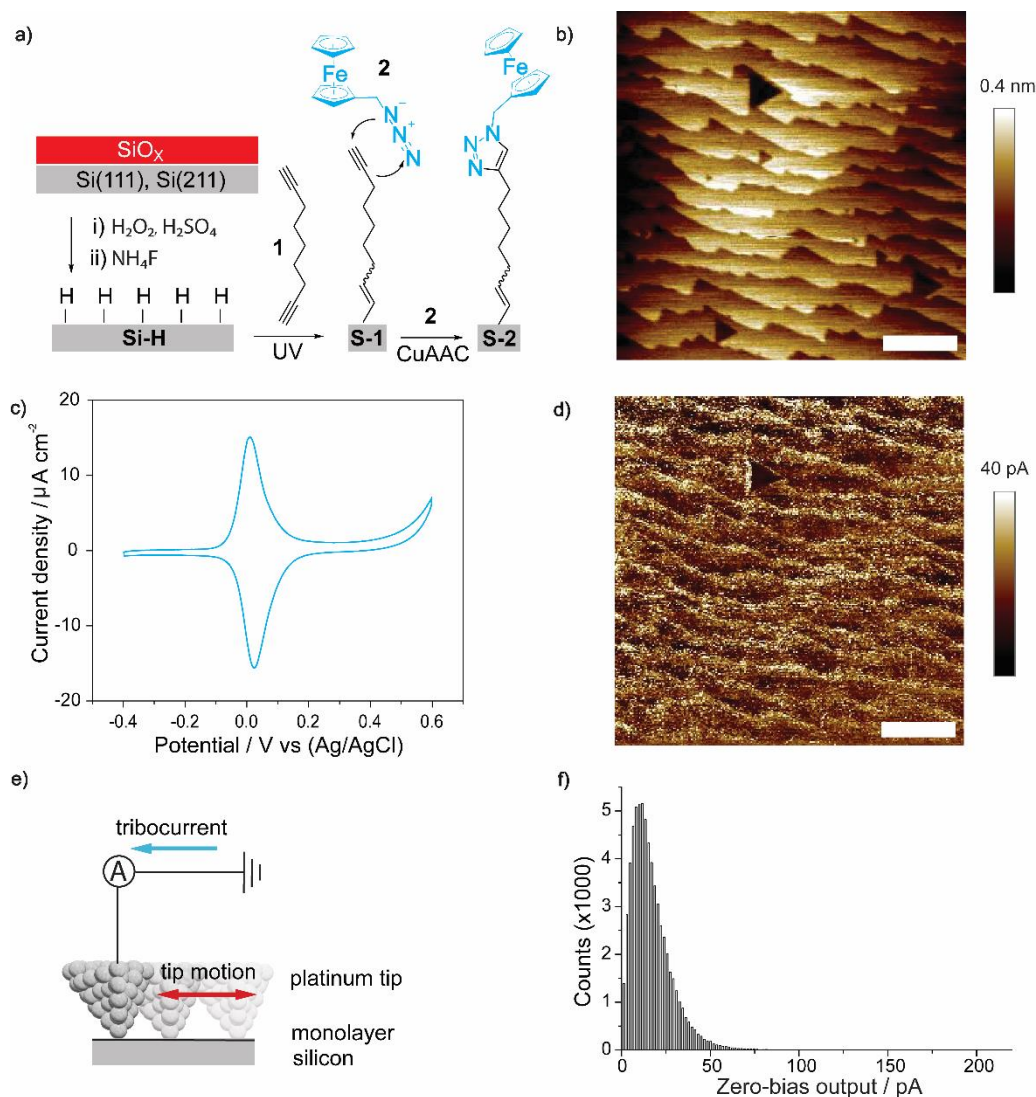
Figure 1. (a) Schematics of the chemical strategy for silicon surface passivation and functionalization. Etching of the native oxide layer was followed by the UV-assisted hydrosilylation of diyne **1** on the hydrogen-terminated silicon (Si–H) surface. The resulting alkyne-terminated monolayer (**S-1**) is then reacted with azide **2** via a Cu(I)-catalyzed alkyne–azide cycloaddition (CuAAC) reaction, to yield a redox-active monolayer (**S-2**). (b) High resolution AFM topography image for a **S-1** monolayer on Si(111). The etching time was 13 min [40% aqueous NH_4F under ambient light (0.2 mW cm^{-2})]. (c) Representative cyclic voltammogram (CV) for a **S-2** sample made on a Si(111) photoanode (100 mV/s, 1.0 M $HClO_4$). The electrode was illuminated at a light intensity of 1.7 mW cm^{-2}. (d) Zero-voltage bias C-AFM map of a **S-1** Si(111) sample. Horizontal scale bars in (b, d) are 1 μm. (e) Schematic representation of the TENG design, made up of an AFM platinum tip sliding over a monolayer-coated silicon wafer. (f) Histogram plot of the current output of the C-AFM map in (d) where the counts indicate the number of pixels (sample locations) of a given current, with a total of ~65k pixels making up a C-AFM map.

near-to-ideal voltammetry (**S-2** samples), along with a smooth surface on which to test current outputs of sliding Si(211)–monolayer–platinum Schottky diode TENGs (**S-1** and **S-2** samples). Throughout this report we have benchmarked our results for Si(211) against those for monolayer

5

systems prepared on Si(111) (Figure 1b–d, f). As mentioned in the introduction, unlike Si(211), the surface chemistry and electrochemistry of Si(111) have been explored extensively.[30, 31]

Since silica and silicon are etched by ammonium fluoride solutions at significantly different rates,[32,33] etching experiments were therefore preceded by ellipsometric measurements to estimate the thickness of the native oxide in the commercial wafer. In our Si(111) wafers the oxide layer was generally ~1 nm, while only slightly thicker (~2 nm, vide infra) for Si(211). Figure 1b gives an example of topography map for a **S-1** sample made on hydrogen-terminated Si(111). The surface is an ensemble of flat ⟨111⟩ terraces separated by small vertical steps (~3 Å).[34] The surface is very smooth, with a root-mean-square (rms) roughness of only 0.2±0.7 nm. The high surface quality is also reflected in the lack of phase angle dispersion at low frequency in electrochemical impedance spectroscopy (EIS) measurements (Figure S1, Supporting Information).[35] At low AC frequencies the EIS phase angle for **S-1** samples approaches −90º, which is an indication of negligible monolayer imperfections.[36] As shown in Figure 1c, the cyclic voltammetry (CV) response of **S-2** samples prepared on Si(111) is close to ideal.[37-39] The full width at half maximum (fwhm hereafter) of the CV current waves is 90.6±3.9 mV. This fwhm is an excellent match of the value expected from a Langmuir isotherm of a Nernstian process. Due to its photoanodic nature, n-type silicon is in depletion, and sample illumination with visible light is required to remove a kinetic barrier and allow the ferrocene redox chemistry to take place within a solvent-accessible potential window.[40, 41] Unlike analogous systems prepared on highly doped p-type silicon, hence operating under accumulation, the CVs of the illuminated n-type photoanodes display a marked cathodic shift in the ferrocene apparent formal potential (Figure S2, Supporting Information). The surface coverage of ferrocene units in **S-2** samples prepared on Si(111), obtained from the CV-derived faradaic charge, was $(2.1\pm0.3) \times 10^{-10}$ mol cm^{-2}. This coverage is lower than the maximum

value for a packed ferrocene monolayer (4.5×10^{-10} mol cm^{-2}),[42] but as expected for a two-step derivatization procedure.[26, 43]

Furthermore, as immediately appreciable from the negligible voltammetric peak-to-peak separation (Figure 1c), the electrode kinetics for **S-2** samples on Si(111) is fast. The peak-to-peak separation for the CVs recorded at 100 mV/s (Figure 1c) becomes more significant at faster voltage sweep rates (Figure S3, Supporting Information). The electron transfer rate constant, k_{et}, extracted from EIS experiments carried out at a DC bias equal to the ferrocene apparent formal potential (Figure S4, Supporting Information) was $(3.6\pm1.4) \times 10^2$ s^{-1}.

Moving now to "dry" sliding junctions, Figure 1d shows a representative zero-voltage bias conductive atomic force microscopy (C-AFM) map for a **S-1** sample made on Si(111). In this experiment the solid platinum AFM tip moves along the **S-1** surface and generates a DC current,[14, 15] that is, a sliding Schottky diode that outputs a DC tribocurrent without an external voltage bias (Figure 1e). A histogram of the DC current mapped in Figure 1d, reveal a skewed shape (Figure 1f), where the most frequent output is around 20 pA, the current range from noise level (~120 fA) to ~220 pA, and with the 99th percentile of the DC current output being 54 pA.

This tribocurrent has the sign of a leakage current (electrons flowing from the metal to the n-type silicon) and is distributed within a relatively narrow range (Figure 1f). The measurable current increase, present near the edges of the Si(111) terraces (Figure 1d), is of unclear origin but it may be linked to the presence of highly conductive $\langle 211 \rangle$ steps separating the $\langle 111 \rangle$ terraces.[16] This localized increment in tribocurrent output is however not reflected in the narrow dispersion (fwhm) of the macroscopic CV measurements, which as discussed above, is close to ideal.

Following this initial electrochemical and electrical benchmarking of Si(111) we then moved to the focus of this study: Si(211), both as electrode as well as TENG substrate. To ensure the
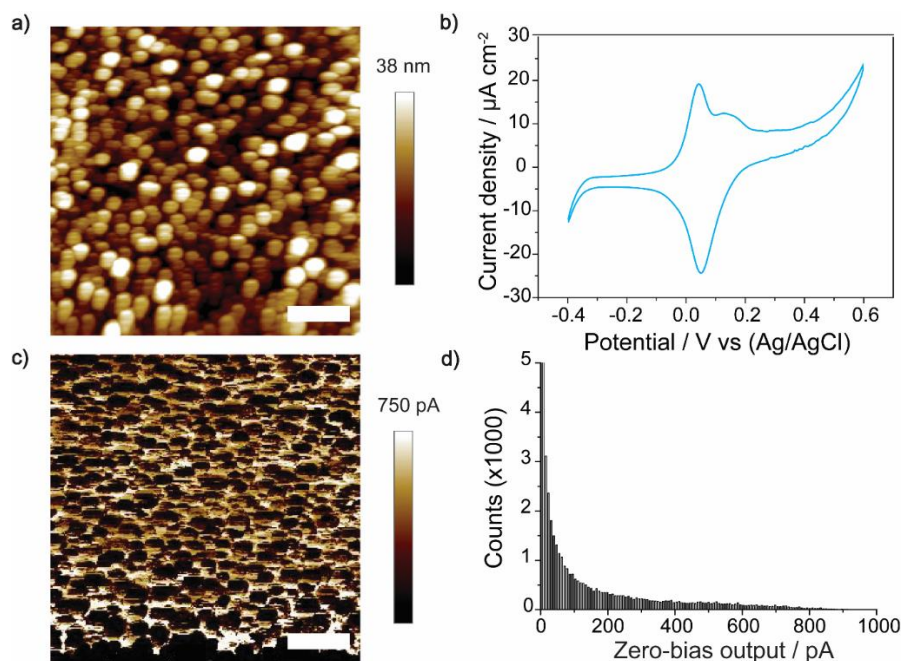
Figure 2. (a) AFM topography image of a **S-1** sample made on Si(211). (b) Representative CV for a **S-2** sample (Si(211), 100 mV/s, 1.0 M HClO$_4$, red light at 1.7 mW cm^{-2}) etched following identical conditions as Si(111). (c) Zero-bias C-AFM map of a **S-1** sample–platinum junction. Horizontal scale bars in (a, c) are 1 μm. (d) Histogram plot of the current output of data in (c). Counts indicate the number of pixels of a given current bin, with a total of ~65k pixels being sampled in a single C-AFM map. Data in figure are for Si(211) wafers etched for 13 min in aqueous 40% ammonium fluoride under ambient light (0.2 mW cm^{-2}) and then chemically modified.

reproducibility of our etching conditions, especially with regards to experiments using shorter etching times, we performed ellipsometric measurements on commercial Si(211) wafers to measure the thickness of the native oxide layer. The oxide on Si(211) was ~2 nm thick, hence prompting us to initially adopt the same etching times used for Si(111). Immersion of Si(211) wafers in degassed 40% aqueous ammonium fluoride for 13 min led however to a rms surface roughness of 7.8±3.2 nm (Figure 2a, **S-1** samples), which is significantly greater than for Si(111). In addition, XPS data (Figure S5, Supporting Information) reveals minor traces of substrate oxidation.

The poor etching outcome is probably caused by the sizable evolution of hydrogen gas on Si(211). Evolution of hydrogen gas during silicon etching is well-known.[44, 45] The etching reaction is affected by several factors, such as the presence of a voltage bias, electrode illumination and

8

doping level,[46] but under identical etching conditions gas evolution is much more evident on Si(211) than on Si(111), resulting in a significantly faster etching rate for the former. This is possibly linked to the higher surface energy of high Miller index silicon surfaces, namely ⟨211⟩, ⟨311⟩, ⟨331⟩,[47] as well as to the lower work function of Si(211) compared to Si(111) and Si(100).[19]

The issue of surface-pinned gas bubbles is probably also exacerbated by a rough surface, further slowing down the desorption kinetics of bubbles.[48] We note that roughening of Si(211) during fluoride etching is not a significant problem in p-type substrates,[20] indicating that etching rates (hence hydrogen evolution) are probably augmented by the electron-donor nature of the n-type samples of this study.[49]

Surface derivatization of these Si(211) rough surfaces, to generate ferrocene-terminated electrodes (**S-2**), led to a relatively large coverage $(2.9 \pm 0.9) \times 10^{-10}$ mol cm^{-2}, as well as to non-ideal CVs shapes with evident multiple peaks (Figure 2b). Peak multiplicity may be triggered by heterogeneous photocurrent effects or by molecular disorder.[50,51] The unusual onset of a Faradaic current below −0.3 V (Figure 2b) is attributed to the minor presence of oxide, introducing energy levels in the gap.[52] It is at first counterintuitive to link an increase in current with silica-related defects. However, despite being counterintuitive, transient increases in conductivity for minor levels of silicon oxidation are known.[24, 53]

Figure 2c shows the corresponding zero-bias C-AFM map. On Si(211) there is a dramatic increase in current output compared to Si(111), with an output average of ~250 pA, and 1% of the sampled locations showing DC currents with values above 870 pA. The distribution of the current output (Figure 2d) indicates however a high frequency of sample locations with output close to noise level. This is significantly different from Si(111), where the most frequent output was around 20 pA.

What followed was an attempt to mitigate the formation of surface-pinned bubbles on Si(211), first by reducing the surface tension of the etchant. Figure S6 (Supporting Information) shows the effect of adding 10% methanol to the aqueous 40% NH$_4$F, with the etching still carried out for 13 min and under ambient light. Addition of methanol to the aqueous NH$_4$F led to a significant roughness reduction: from ~8 nm to 3.2±0.3 nm. This can be explained by a reduction in the water surface tension, preventing the nucleation and growth of surface-pinned gas bubbles (Figure S6). Further improvement was obtained by shortening the etching time to 2 min, resulting in a rms roughness of only 0.9±0.1 nm (Figure S7, Supporting Information).

Such improvements in topography were however not paralleled by a reduction in electrochemical non-idealities. CVs for **S-2** Si(211) photoanodes prepared under the above (partially improved) etching conditions are shown in Figure 3a,b. For the shorter etching time (2 min) there is no peak multiplicity, but CV waves are broad (fwhm ~208 mV, Figure 3a). This indicates a negative value of the Frumkin G parameter. Negative G values are an indication of net repulsive forces between the redox units,[54-56] but it is surprising since the ferrocene coverage (2.8±0.7) × 10^{-10} mol cm^{-2}, is comparable to that of Si(111) samples. Roughness factors could be behind the increased repulsions between ferrocene units. Longer etching times (13 min) lead once again, despite the smoother surface relative to the results for samples etched in absence of methanol (Figure 2), to multiple CV peaks (Figure 3b). As mentioned above, an heterogeneous redox population can manifest as multiple peaks.[50]
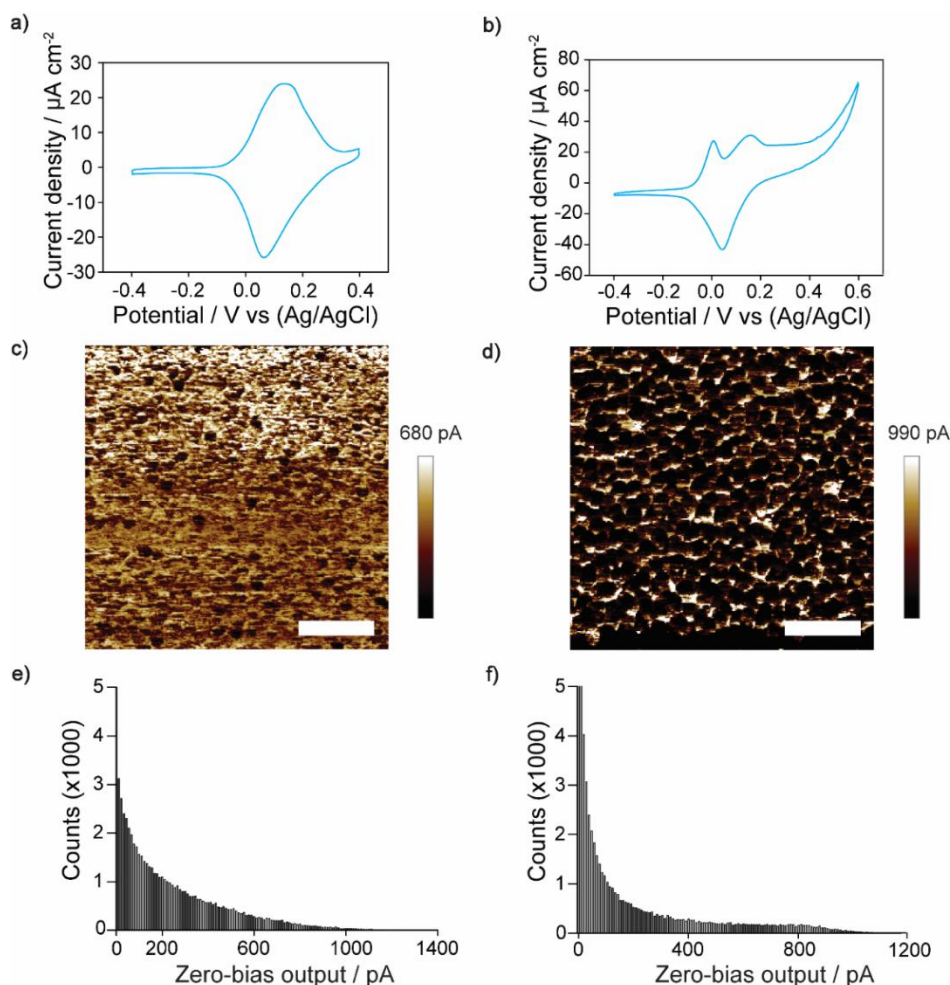
Figure 3. (a, b) Representative CVs for Si(211) **S-2** photoanodes (100 mV/s, 1.0 M HClO$_4$, 1.7 mW cm^{-2} red light electrode illumination). Samples were etched in a mixture of MeOH and 40% NH$_4$F (1:10) under ambient light (0.2 mW cm^{-2}). The etching time varied between 2 min (a) and 13 min (b). (c, d) Zero-bias C-AFM experiments carried out on **S-1** samples etched for 2 min (c) and 13 min (d). Horizontal scale bars in (c, d) are 1 μm. (e, f) Histograms of the current output of the C-AFM maps in (c, d). Counts are in pixels (~65k total image pixels).

Ferrocene coverages scaled with etching times, reaching values as high as (4.9±0.2) × 10^{-10} mol cm^{-2} (13 min). This is probably not a true increase in surface coverage but more likely due to an increase in actual electrode area with increased roughness (Figure S7, Supporting Information). XPS data (Figure S8, Supporting Information) for samples prepared when methanol is added to the etchant indicate small traces of silicon oxide.

C-AFM performed on these samples (Figure 3c,d) revealed again large maximum tribocurrent outputs, but the most frequent value is still close to noise level. Despite the significant improvement in surface smoothness, histograms in Figure 3e,f show a current distribution very similar to that of samples etched in absence of methanol (Figure 2d). The 99th percentile of the

current output is 1.2 nA for the 2 min etching, and 915 pA for samples etched for 13 min. Further, for both the data of Figures 2 and 3, non-ideal cyclic voltammetry responses seem to be linked to the likelihood of having a large fraction of the sample outputting tribocurrent close to noise. Whether electrochemical non-idealities could be used to predict if a given surface will perform poorly in a TENG design is what we next tried to clarify.

Considering the anodic nature of etching process, and since we are focusing on n-type electrodes (photoanodes), we attempted slowing down the etching rate by shielding the electrodes from light. Under dark, adding methanol to the etching bath, and by further adjusting the etching times, we were able to reduce the presence of surface-pinned bubbles and improve surface smoothness. Samples etched for 13 min in a mixture of MeOH and 40% NH_4F (1:10) while protected from light had a rms roughness of only 2.6±0.1 nm (Figure S9, Supporting Information). This is a significant improvement compared to our initial results (Figure 2) and closer to the quality of the Si(111) benchmark (Figure 1). The outcome (surface roughness) of the various etching conditions explored in this work is summarized in Table S1 (Supporting Information). Again, samples etched for 2 min were very smooth, with an average roughness of only 0.7±0.4 nm.

The quality of the carbonaceous monolayer on Si(211) is also comparable to what can be achieved on Si(111). C 1s and Si 2p XPS data, such as those of Figure 4a,b, suggest that in Si(211) **S-1** samples ~27% (13 min etching) of the silicon surface atoms bear a monolayer-forming molecule (25% for the 2 min etching),[57] with no clear traces of substrate oxidation.

A satisfactory fitting of the C 1s XPS emission (**S-1** samples) required three contributions: one for carbon bound to silicon at 283.6 eV,[58] a carbon-bound carbon envelope at 284.9 eV,[59] and a high binding energy band at 286.9 eV, ascribed to C≡C and/or C−OH.[60] Elemental silicon emissions are found at 99.5 eV for Si $2p_{3/2}$ and at 100.1 eV for Si $2p_{1/2}$. The high binding energy
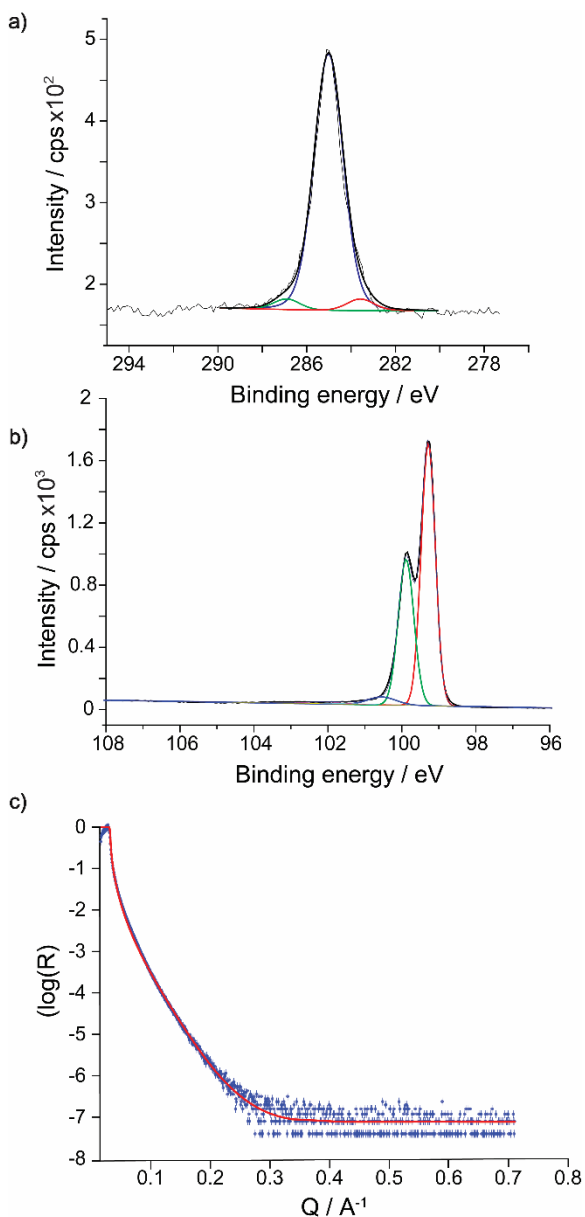
Figure 4. (a, b) C 1s and Si 2p high-resolution XPS scans of **S-1** samples grafted on Si(211) [dark etching in 1:10 v/v MeOH/NH$_4$F, 13 min]. (c) XRR spectra for **S-1** samples [Si(211), etching as in (a, b)]. The refined data (red solid line, $\chi^2 = $ ~30) is plotted over the experimental data (solid blue symbols).

Si 2p signal shifted by 0.40 eV from the bulk Si 2p$_{1/2}$ peak, discernible in the high-resolution Si 2p scans (Figure 4b), is a common XPS feature even in oxide-free samples and is tentatively ascribed to silicon bound to hydrogen.[61]

Ferrocene-terminated (**S-2**) samples prepared on Si(111) and Si(211) electrodes returned similar XPS spectral features, including similar levels of oxidation (Figure S10, Supporting Information).

The successful attachment of the ferrocene unit was reflected by the appearance of Fe 2p signals at ~710–720 eV and N 1s at ~401 eV. The experimental binding energies are in good agreement with those reported for other immobilized triazoles.[28] The XPS narrow scan of the Fe 2p region (Figure S10c,d) shows two main spin–orbit-split components, Fe $2p_{3/2}$ and Fe $2p_{1/2}$, located at 708.6 and 721.5 eV respectively, indicating a predominant Fe(II) population. There are traces of high-binding energy satellite signals indicating the presence of Fe(III) species, hence a non-negligible level of oxidation of ferrocene to ferricenium units. The N 1s signal was fitted in two contributions assigned to N—$\underline{N}$=N (400.7 eV) and $\underline{N}$—N=N (402.3 eV), with the area ratio of the two envelops being ~ 2:1, as expected for a triazole moiety. The deconvolution of the N 1s signals is supported by data for nitrogen atoms of aromatic compounds.[62] Absent from the N 1s spectra is the high binding energy emission (~405 eV) from the central and electron-deficient nitrogen atom unreacted azidomethylferrocene **2**, hence supporting negligible physical adsorption of the unreacted azide in the **S-2** film.

Electron density (ρ_{el}) of the organic monolayer [**S-1** film made on Si(211)], inferred from the refinement of X-ray reflectometry (XRR) data (Figure 4c), was 0.35 $e^{-}/Å^{3}$, which is not drastically lower than the 0.44 $e^{-}/Å^{3}$ for the same film prepared on Si(111) (Figure S11 and Table S2 Supporting Information). Literature values for ρ_{el} of high-quality carbon-based films made on oxide-free silicon range, in general, between 0.32 and 0.46 $e^{-}/Å^{3}$.[63, 64] The XRR-derived roughness of the monolayer–air interface was ~3.1 nm, and very close to the AFM-derived value (13 min etch).

S-2 samples made on dark-etched Si(211) wafers showed a nearly ideal voltammetric fwhm (Figure 5a,b). Furthermore, for samples etched for 13 min the ferrocene coverage was $(2.0\pm0.2) \times 10^{-10}$ mol cm^{-2}, a value comparable to the Si(111) benchmark (Figure 1) but likely to reflect an
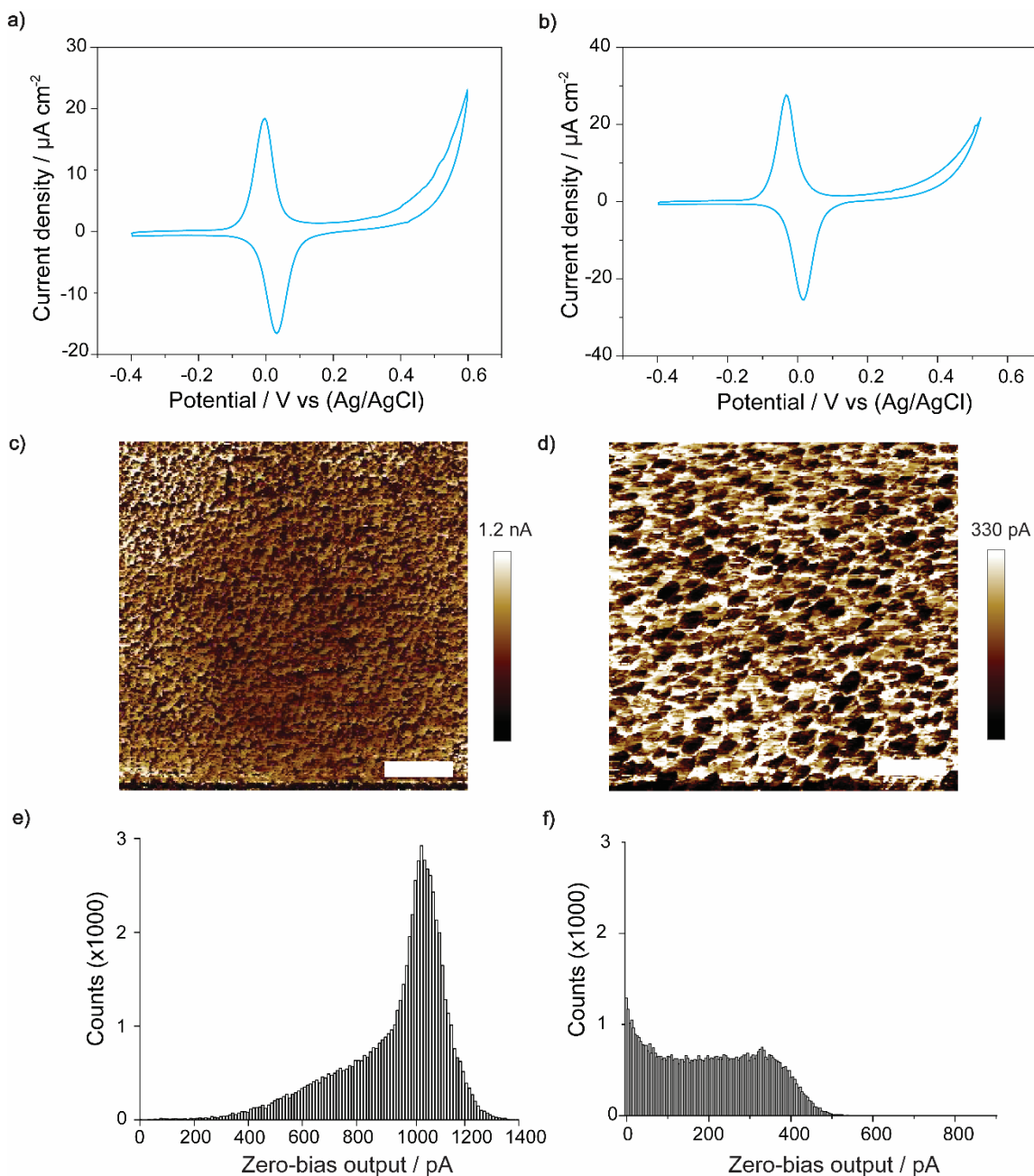
Figure 5. (a, b) Representative CVs for Si(211) **S-2** photoanodes (100 mV/s, 1.0 M HClO$_4$, 1.7 mW cm^{-2} red light electrode illumination). Samples were etched in a mixture of MeOH and aqueous 40% NH$_4$F (1:10, v/v) in dark. The etching times were 2 min (a) and 13 min (b). (c, d) Zero-bias C-AFM maps [**S-1**, etching time 2 (c) and 13 min (d)]. Horizontal scale bars in (c, d) are 1 μm. (e, f) Histograms of the tribocurrent output from the C-AFM experiments [2 min, (e); 13 min, (f)] respectively. Counts are in pixels (~65k total image pixels).

actually lower molecular density as the Si(211) roughness (13 min etch time) is significantly higher than that of Si(111) samples. Lower coverages were obtained for the smooth Si(211) surfaces (2 min etch), which were on average (1.2±0.1) × 10^{-10} mol cm^{-2}, roughly half the Si(111) value. We

15

are at present unsure on the cause of the lower ferrocene coverage, as the nonadiyne coverage (vide

supra, XPS data) of the base acetylene layer appears to be comparable between the 2 and 13 min

samples. Furthermore, etching times of 6 and 10 min led to qualitatively similar CVs, with the

ferrocene coverage per geometric area scaling with the etching time (Figure S12, Supporting

Information). As expected, the anodic and cathodic peak currents scaled with the scan rate, and

not with the square root of the scan rate, indicating a surface-confined (diffusionless) redox process

(Figure S13, Supporting Information).

Notably, as evident in Figure 5a,b, the CVs of **S-2** samples made on etching-optimized Si(211)

are characterized by a peak inversion: at low voltage sweep rates the anodic wave peaks at voltages

more negative than those of the cathodic wave maxima. This unusual feature is not an artifact, but

an indication of electrostatic interactions between the positively charged ferricenium units and the

semiconductor space-charge layer (SCL). CV inverted peak positions disappear at larger voltage

sweep rates (Figure S14, Supporting Information) as the peak inversion becomes masked by

kinetic factors.[37, 38] The CV current is always the net sum of anodic and cathodic currents, but the

appearance of this peak inversion indicates that dynamic charges in **S-2** samples (the positive Fc^+

surface tethers formed upon Fc oxidation) transiently remove a barrier (the upward SCL band-

bending) sensed by electrons crossing from the silicon to the electrolyte, hence transiently favoring

the photogenerated cathodic current. As a result, the cathodic wave peaks at more positive voltages

than the anodic wave. Interestingly, the peak inversion is much more evident on Si(211) than on

Si(111), where it manifests only occasionally. Although a complete explanation is still lacking,

this electrostatic effect is possibly linked to disorder in the molecular film, and/or to the presence

of low levels of oxide not detectable by XPS. The oxide may decrease the dielectric barrier

(relative to a well packed organic monolayer) which possibly favors the electrostatic interactions

behind the inversion. In support of disorder in the monolayer being linked to the inverted peak positions is the consistent appearance of such phenomenon in amorphous Si.[37]

When the voltage sweep rate is increased (Figure S14), or upon substrate oxidation when charge-transfer kinetics is irreversibly slowed down,[65] such peak inversion is no longer detectable (Figures S15–S16, Supporting Information). We propose that such disappearance can be turned into a simple diagnostic tool of substrate oxidation, and as discussed below, it has an immediate implication in anticipating the performance of a TENG made on these substrates.

The outcome of C-AFM experiments on Si(211) **S-1** samples are shown in Figure 5c–f. TENGs made on **S-1** samples etched for 2 min led to excellent outputs, with the mode of the zero-bias tribocurrent being at 1.1 nA (equivalent to a current density of 1.2×10^7 A/m^2) (Figure 5e). As clearly visible in the current histogram of Figure 5f, **S-1** samples made on Si(211) etched for 13 min had a large fraction of spots with tribocurrent close to noise level, but also an almost equally large population of locations with very high current output (~320 pA), and with a satisfactory homogeneity across the macroscopic sample (Figure S17, Supporting Information). This is a remarkable improvement over Si(211) etched under ambient light. The 99th percentile of the current output is 1.2 nA and 528 pA, for the 2 and 13 min samples, respectively. Such high current outputs, along with well-defined voltammetric responses (Figure 5a,b), are a significant improvement against more widespread Si(111) systems, which we initially took as our benchmark (Figure 1).

Further, the current output of the sliding junction was tested under prolonged operations (Figure S18, Supporting Information), as well as under different scan speeds (Figure S19, Supporting Information). There is a substantial drop in the mean zero-bias current with consecutive cycling

(~90% after three full scans). This is probably caused by deterioration of the monolayer and anodic damaging of the substrate.

Changes to the platinum sliding velocity revealed that the output current increases with scan speed (Figure S19, Supporting Information). We are unsure of the reason of such positive correlation between sliding velocity and current, but we believe it may be linked to a not yet explored flexoelectric time factor, such as electrons accumulating on one side of the junction, inside a well created by bands that are being bent under pressure, eventually drifting away anisotropically before being transferred directionally from the metal to the semiconductor. This point will need further investigation. Furthermore, as shown in Figure S20 (Supporting Information) we found a direct correlation between force and DC current output. Changes to the applied load have recently been demonstrated to influence the DC output of similar metal–semiconductor systems.[23] We believe this increase not only to reflect increased friction due to increased normal force, but also to be a response to dynamic changes to the band-bending upon inevitable fluctuations to the vertical load. The contribution of flexoelectric effects to triboelectricity has been recently demonstrated and explained by Marks and co-workers.[25] For a contact between a platinum–iridium ($Pt_{0.8}Ir_{0.2}$) AFM tip and a niobium-doped strontium titanate surface, flexoelectricity is rationalized as a band-bending ratcheting mechanism cyclically moving electrons from the semiconductor into the metal under cyclic changes to the contact pressure. It is likely that a similar mechanism will hold for silicon–platinum junctions, but a direct test of this hypothesis is still lacking.

Since the formation of the triazole moiety has been shown to cause a reduction in work function, to increase leakage current and to enhance tribocurrents,[15] we also tested the zero-bias current output of sliding junctions made on **S-2** samples. C-AFM experiments performed on **S-2** surfaces
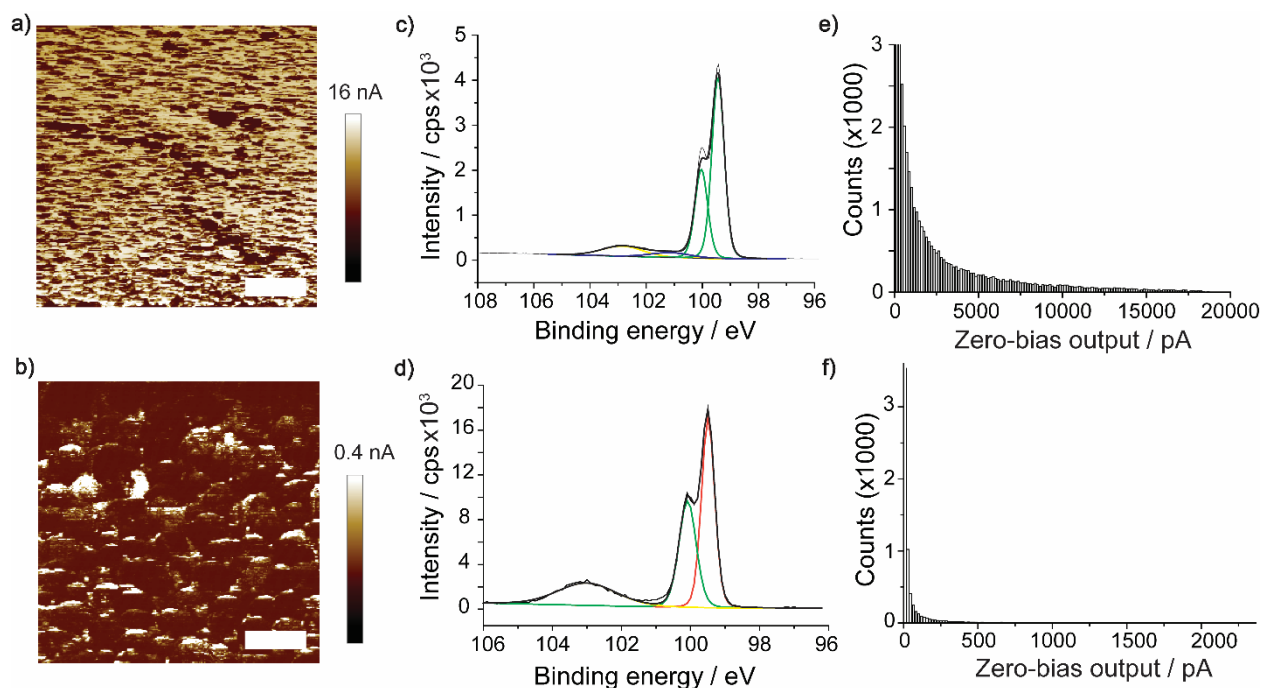
Figure 6. (a, b) Zero-bias C-AFM maps for Si(211) **S-1** samples etched for 13 min in a mixture of MeOH and aqueous 40% NH$_4$F (1:10, v/v) under dark. Samples were subjected to 10 (a, c, e) and 40 (b, d, f) CV cycles from −0.4 to 0.6 V, 100 mV/s, 1.0 M HClO$_4$, 1.7 mW cm^{-2} red light electrode illumination, and horizontal scale bars in (a, b) are 1 μm. (c, d) XPS Si 2p high-resolution, scans of the anodically damaged samples (10 and 40 CV cycles, (c) and (d) respectively). The broad band between 101 and 104 eV are photoelectrons from Si$^{(1)}$ to Si$^{(4)}$ oxides. (e, f) Histograms of the current output from the C-AFM experiments of (a) and (b). The counts are in pixels (~65k total image pixels).

revealed for both facets an increase in current outputs relative to **S-1** samples. Outputs were as high as 8 nA for Si(111) (99th percentile of 3.8 nA) (Figure S21, Supporting Information) and 10 nA for Si(211) (99th percentile of 9.8 nA) (Figure S22, Supporting Information).

To clarify further on why such large TENGs current and why the occurrence of bimodal distributions, we focused on the impact of oxide growth on these surfaces. We therefore performed C-AFM experiments on a deliberately oxidized samples. Figure 6a is a C-AFM map recorded on a sample first subjected to 10 CV cycles. The 99th percentile of the tribocurrent output was as high as 14 nA (current average ~2.8 nA). There is an oxidative damage (Figure 6b), and yet a significant tribocurrent enhancement relative to freshly-prepared samples (Figure 5). After 40 CV cycles (Figure 6b) TENG performances drop drastically. As oxide grows beyond trace levels, as shown

in Figure 6d and Figure S23 (Supporting Information), the value of 99th percentile current output

drops to 1.8 nA (the average current decreases to ~287 pA).

Upon sample oxidation there is an increase in the fraction of sample locations that have very

low or negligible zero-bias tribocurrent (Figure 6e,f) but while this is not surprising since silica is

an electrical insulator, what is notable is that minor silica growth result in an increase of the

maximum TENG output. The explanation is probably that low levels of silica introduce energy

levels in the band gap, causing a couterintuitive increase in conductivity which is however not

unprecedented. For example minor silicon oxidation accounts for an initial and transient drop in

the anodization voltage required for the constant-current growth of silica adlayers over a silicon

electrode.[53]

Conclusions

In this work we have optimized the etching and surface modification of Si(211) – an

underexplored but highly conductive silicon crystal cut. The overall goal is to facilitate the uptake

of silicon as platform for DC triboelectric nanogenerators (DC TENGs). Silicon is a cheap and

readily available semiconductor, and a promising substrate for out-of-equilibrium Schottky diode

TENGs for autonomous power supplies converting microscopic sliding motion into DC

electricity.[66-68] We have shown that the etching of Si(211) in aqueous ammonium fluoride can

yield surfaces as smooth as high quality Si(111) surfaces, which are taken as the benchmark. The

key to achieve this, was to reduce etching rates to a minimum by means of complete shielding

from light, and simultaneously preventing the formation of surface-pinned hydrogen bubbles by

reducing the etchant surface tension. Such optimized Si(211) system can be monolayer modified

and when rubbed with sharp metal contacts yields tribocurrent outputs significantly greater than

equivalent sliding Schottky diodes made on Si(111). We found that monolayer-modified Si(211) systems which upon attachment of a redox tether give broad and multiple voltammetric waves are generally poor TENG performers, while surfaces with well-behaved electrochemistry were the best performers, with negligible fraction of sample locations having tribocurrent outputs close to noise level. Introducing defects in the band gap (namely traces of silica) enhanced significantly the tribocurrent output. This enhancement is however temporary, as further substrate oxidation leads to an increase of the sample's locations with negligible current outputs. The work highlights the scope of non-canonical silicon crystallographic cuts in both TENGs and electrochemistry and reveals the scope of engineering defects in the gap to boost DC TENGs outputs.

Experimental section

Chemicals and materials. Unless stated otherwise, all chemicals were of analytical grade and used as received. Sulfuric acid (95–97%, Honeywell), aqueous hydrogen peroxide (30% w/w, Honeywell), and aqueous ammonium fluoride (40% w/w, Honeywell) were of semiconductor grade or equivalent purity grade. Methanol (HPLC grade, >99.9%), and ammonium sulfite monohydrate (92%) were purchased form Sigma–Aldrich. Hydrochloric acid (35–37%, Ajax Finechem) and 2-propanol (>99.8%, Ajax Finechem) were supplied by Thermo Fisher Scientific. Redistilled dichloromethane (DCM) and Milli-Q™ water (>18 MΩ cm resistivity) were used for wafer-cleaning and surface-modification procedures. Si(111) and Si(211) prime grade single-side polished silicon wafers ($\pm 0.05°$, 500 μm thick), N-type with a resistivity of 7−13 Ω cm, were obtained from Siltronix, S.A.S (Archamps, France). 1,8-Nonadiyne (**1**, 98%, Sigma–Aldrich) was used as received. Azidomethylferrocene (**2**) was prepared according to literature procedures.[28]

Surface modification procedures. Silicon wafers were first cut into either 10 × 10 mm (AFM measurements), 15 × 15 mm (electrochemical measurements and ellipsometry), or 15 × 35 mm (XRR measurements) pieces, then washed sequentially with DCM, 2-propanol, and water before being immersed for 30 min in hot (100 °C) piranha solution [a 3:1 mixture (v/v) of concentrated sulfuric acid and hydrogen peroxide (30%)]. Samples were then rinsed three times with water, and then immediately etched in a deoxygenated (by means of bubbling argon for at least 15 min) aqueous 40% solution of ammonium fluoride. A small amount of ammonium sulfite was added as an oxygen scavenger to the etching bath. Etching times, presence, or absence of methanol, and degree of illumination of the sample during the etching, were varied and are specified separately. Control Si(111) samples were etched for 13 min under ambient light with the polished side facing up (fluorescent tubes, 0.2 mW cm^{-2}). Hydrogen-terminated samples (Si–H) were then rinsed once with Milli-Q water, twice with DCM, and then blow-dried under a stream of nitrogen. The Si–H surfaces were immediately reacted with a small sample of 1,8-nonadiyne (**1**, Figure 1a) following minor modifications of a previously reported hydrosilylation procedure. A brief account of the hydrosilylation procedure is as follow: the liquid diyne stock was bubbled with argon for at least 15 min, then ~0.1 mL of **1** was used to cover a Si–H sample, which was then rested for 2 h under nitrogen at approximately 20 cm from a 312 nm light source (Vilber, VL-215.M, nominal power output of 30 W). The surface of the liquid sample was covered with a 1 mm thick quartz plate (part 01031-AB, SPI Supplies) to limit its evaporation. The reaction was stopped by removing the acetylene-terminated monolayer (**S-1**) from the UV chamber, followed by extensive sample rinsing with DCM. **S-1** samples were stored for 24 h under DCM at +4 °C prior to analysis or further derivatization. The copper (I)-catalyzed azide−alkyne cycloaddition (CuAAC) reaction used to prepare a ferrocene-functionalized silicon surface (**S-2**), was performed following previous

procedures.[28] **S-1** were rinsed with 2-propanol, then placed in a reaction tube containing 4 mL of azidomethylferrocene (**2**) in 2-propanol (0.5 mM), 1 mL of aqueous copper sulfate (20 mol % relative to **2**), and 1 mL of aqueous sodium ascorbate (100 mol % relative to **2**). The reaction tube was stoppered, and the CuAAC reaction carried out at room temperature, with gentle agitation while shielded from ambient light. The reaction was stopped after 30 min by removing the ferrocene-modified electrode (**S-2**) from the vial. Samples were rinsed thoroughly with 2-propanol, water, HCl (0.5 M) and DCM. Finally, samples were dried under a stream of nitrogen gas before being analyzed.

Atomic force microscopy. Atomic force microscopy (AFM) measurements of surface topography and zero-bias tribocurrent were carried out on a Park NX10 (Park Systems Corporation, Korea). The instrument is fitted with a variable enhanced conductive (VECA) probe holder for the conductive AFM (C-AFM). The AFM tips were solid platinum tips (25Pt300B, Rocky Mountain Nanotechnology, Holladay) with a resonance frequency of 14 kHz, a spring constant of 18 N/m, and a tip radius of ~18.20 nm. The experimental contact area (tip–sample) was in the range 2.4–5.5 nm^2 and was calculated as described in the Supporting Information (Section S1). All measurements were performed at room temperature and under ambient air (RH of ~76%). Topography and current images were obtained simultaneously. The C-AFM sample routing is such that a positive-sign electric current indicates a tip-to-silicon electron flow (i.e., a leakage current for n-type Si with a Pt top contact). Samples were secured on the AFM stage by carbon tape after having ensured ohmic contact between sample and stage by scratching the back of the silicon with SiC emery paper and applying on the abraded surface a small amount of gallium-indium eutectic (99.9% Alfa Aesar). Unless otherwise specified the imaging size was set to 5×5 μm, the imaging resolution to 256 points/line, the scan rate to 1.0 Hz, and the applied normal force to 360 nN. All

data were analyzed with XEI processing software (Park Systems), average and maximum current output results are the average of at least three independent measurements. Maximum zero-bias current at the 99th percentile sampled points at zero-bias, states for current outputs higher than 99% of the total sampled points.[69] The vertical palette color legend (scale bar) for the AFM height and current maps does not cover the full scale. The scale bar maximum was selected so to better visualize lateral changes in the current and height images. The residual output (noise level) is situated around ~120 fA.

Electrochemical measurements. All electrochemical measurements were carried out on a CHI650D electrochemical workstation (CH Instruments, Austin) and using a three-electrode and single-compartment polytetrafluoroethylene cell. Monolayer-modified **S-1** and **S-2** surfaces (10 × 10 mm) served as the working electrode, a platinum coil as the counter electrode, and an Ag/AgCl (in 3.0 M aqueous NaCl solution) as potential reference. The geometric area of the working electrode was set to 0.28 cm^2 by means of a circular rectilinear cross-section Kalrez® gasket. Electrical contact of the working electrode to a copper plate was obtained as described for the C-AFM experiments. The electrolyte was aqueous 1.0 M perchloric acid, and all measurements were carried out in air at room temperature (22±2°C) and under illumination. The red light illuminating the silicon electrode, through the electrolyte compartment, was a LED (660 nm, nominal power output 940 mW, Thorlabs part M660L4) coupled to a collimator adapter (SM1P25-A, Thorlabs) The collimator–sample distance was approximately 10 cm. A meter from Amprobe, model (IC-LM-200) was used to measure the illuminance. Electrode illumination was measured in lx but reported in mW cm^{-2} (1 lx approximated to 0.00). The light intensity at the electrode surface was generally ~1.7 mW cm^{-2}. Surface coverages of ferrocene molecules on **S-2** samples are reported in mol cm^{-2}. Coverage values are calculated from the CV-derived faradaic charge, taken as the

average of the anodic and cathodic scans background-subtracted integrated current. Reported data are the average of at least three independently prepared and analyzed samples, with values averaged over at least 10 different voltage sweep rates. The 99% confidence limit of the mean coverage was calculated following literature procedures. The apparent electron-transfer rate constants, (k_{et}), for the electron-transfer reaction between ferrocenes and substrate (**S-2** samples) was estimated from EIS measurements using the formalism developed by Laviron.[70] EIS data to estimate k_{et} were obtained at a working electrode DC bias, E_{dc}, equal to the mid-point between the potential of the anodic and cathodic current peaks from CV experiments. The k_{et} was calculated as $1/(2\ R_{et}C_{ads})$. The potential amplitude of the AC perturbation was set to 15 mV. EIS data were collected between 10^5 and 10^0 Hz. Data were analyzed with ZView (Version 4.0c, Scribner Associates) and using the equivalent circuits shown in Section S2 (Supporting Information). Reported values are the average of at least three independently prepared and analyzed samples.

X-ray photoelectron spectroscopy. X-ray photoelectron spectroscopy (XPS) was used to analyse the atomic composition and chemical state of elements in the monolayers. An AXIS Ultra DLD spectrometer (Kratos Analytical Inc., Manchester, UK) with a monochromic Al Kα radiation (1486.6 eV) and a hemispherical analyser (165mm radius) was operated in Fixed Analyser Transmission (FAT) mode, at 2×10^{-8} Torr. The analysis area was 300×700 μm and the photoelectron take off angle was perpendicular to the sample. Survey spectra were obtained from the accumulation of 5 scans using 160 eV pass energy over a 0–1100 eV range in 0.5 eV steps. High resolution spectra (10 scan accumulations) were collected at a pass energy of 20 eV, with a step size of 0.05 eV for Si 2p (96–108 eV) and 0.1 eV for C1s (278–295 eV). High resolution narrow scans for O 1s (520–545 eV), N 1s (395–407 eV) and Fe 2p (700–735 eV) were collected in normal emission with a monochromatic Kratos Axis Supra, using Al K-alpha excitation (1486.7

eV) at 225 W. The pass energy was set to 20 eV, the step size to 0.05 eV and the dwell time to 200 ms. XPS data was processed using CasaXPS software. Analysis of the spectra involved background subtraction using the U2 Tougaard routine and Lorentzian-Asymmetric (LA, 1.53,243) line shape. All the reported energies are binding energies (eV) and corrected by applying a rigid shift to bring the Si $2p_{3/2}$ emission to 99.5 eV.

X-ray reflectometry. Specular X-ray reflectometry (XRR) of the monolayer-modified sampled was measured on a Panalytical X'Pert Pro instrument. The instrument uses an X-ray wavelength of 1.54 Å (Cu Kα) from a tube source and a Göbal mirror and fixed slit of 0.1 mm to create a parallel beam. Samples had an average size of 15×30 mm^2 and a 10×10 mm^2 illuminated footprint was used. Data were collected over a time frame of 2 h and were taken from an angle of incidence of 0.05° to 5.0° in 0.01° steps with a counting time of 15 seconds per step. Collected data was reduced so the reflectivity at the critical edge is scaled to be unity and angle of incidence converted to momentum transfer ($Q = 4\pi\sin\theta / \lambda$, where θ is angle of incidence and λ wavelength). The prepared organic thin layers structural parameters, were fitted and refined using *refnx* analytical software. The data was fitted to a model that describes the monolayer as a single slab with parameters of thickness, scattering length density (SLD), and roughness. These three parameters were varied along with the background value and substrate roughness using a differential evolution routine until a global minimum in χ^2 was reached. The SLD of the substrate (silicon) was set at 2.01×10^{-5}Å^{-2} during the fitting routines. The experimental data is represented as points, and the theoretical reflectivity develop with the structural models is presented in the form of solid lines.

Ellipsometry measurements. The thickness of the oxide layer (post piranha wash, prior to the fluoride etching) was measured by ellipsometry on a M-2000XI ellipsometer (J.A. Woollam Co.).

The samples were irradiated with a FLS-300, 75 W Xe arc lamp light source working in the UV-visible-NIR (245–1690 nm) at a fixed angle of 65°. Spectra analysis was performed with the CompleteEASE® software (J.A. Woollam).

ASSOCIATED CONTENT

Supporting Information

The Supporting Information is available free of charge on the ACS Publications website.

Additional experimental procedures, AFM data under different scan velocities, different loads, with different organic terminal groups, and scans over large areas. XPS data for alternative etching conditions and surface chemistries, XRR data for large-area roughness measurements and a tabled summary of the outcome from alternative etching conditions. EIS data.

Corresponding Author

Simone Ciampi – School of Molecular and Life Sciences, Curtin Institute of Functional Molecules and Interfaces, Curtin University, Bentley, Western Australia 6102, Australia.

Email: simone.ciampi@curtin.edu.au

Authors

Carlos Hurtado, Xin Lyu, Stuart Ferrie – School of Molecular and Life Sciences, Curtin University, Bentley, Western Australia 6102, Australia

Anton P. Le Brun – Australian Centre for Neutron Scattering, Australian Nuclear Science and Technology Organization (ANSTO), Lucas Heights, New South Wales 2234, Australia

Melanie MacGregor – Flinders Institute for Nanoscale Science and Technology, Flinders University, Bedford Park, South Australia 5042, Australia

Author Contributions

The manuscript was written with contributions by all authors. All authors have approved the final version of the manuscript.

Notes

The authors declare no competing financial interest.

ACKNOWLEDGMENTS

REFERENCES

1.   Peng, K.-Q.; Wang, X.; Li, L.; Hu, Y.; Lee, S.-T. Silicon nanowires for advanced energy conversion and storage. *Nano Today* **2013,** *8*, 75–97.
2.   Fabre, B. Ferrocene-Terminated Monolayers Covalently Bound to Hydrogen-Terminated Silicon Surfaces. Toward the Development of Charge Storage and Communication Devices. *Acc. Chem. Res.* **2010,** *43*, 1509–1518.
3.   Michaels, P.; Alam, M. T.; Ciampi, S.; Rouesnel, W.; Parker, S. G.; Choudhury, M. H.; Gooding, J. J. A robust DNA interface on a silicon electrode. *Chem. Commun.* **2014,** *50*, 7878–7880.
4.   Linford, M. R.; Chidsey, C. E. Alkyl monolayers covalently bonded to silicon surfaces. *J. Am. Chem. Soc.* **1993,** *115*, 12631–12632.
5.   Vogel, Y. B.; Zhang, J.; Darwish, N.; Ciampi, S. Switching of Current Rectification Ratios within a Single Nanocrystal by Facet-Resolved Electrical Wiring. *ACS Nano* **2018,** *12*, 8071–8080.
6.   Ciampi, S.; Darwish, N.; Aitken, H. M.; Díez-Pérez, I.; Coote, M. L. Harnessing electrostatic catalysis in single molecule, electrochemical and chemical systems: a rapidly growing experimental tool box. *Chem. Soc. Rev.* **2018,** *47*, 5146–5164.
7.   Fabre, B.; Pujari, S. P.; Scheres, L.; Zuilhof, H. Micropatterned Ferrocenyl Monolayers Covalently Bound to Hydrogen-Terminated Silicon Surfaces: Effects of Pattern Size on the Cyclic Voltammetry and Capacitance Characteristics. *Langmuir* **2014,** *30*, 7235–7243.
8.   Lattimer, J. R. C.; Brunschwig, B. S.; Lewis, N. S.; Gray, H. B. Redox Properties of Mixed Methyl/Vinylferrocenyl Monolayers on Si(111) Surfaces. *J. Phys. Chem. C*. **2013,** *117*, 27012–27022.
9.   Mukhopadhyay, A.; Bernard, B.; Liu, K.; Paulino, V.; Liu, C.; Donley, C.; Olivier, J.-H. Molecular Strategies to Modulate the Electrochemical Properties of P-Type Si(111) Surfaces Covalently Functionalized with Ferrocene and Naphthalene Diimide. *J. Phys. Chem. C*. **2019,** *123*, 11026–11041.
10.   Zhang, X. G., *Electrochemistry of Silicon and Its Oxide*. Boston, MA: Springer: Boston, MA, 2007.
11.   Ciampi, S.; James, M.; Le Saux, G.; Gaus, K.; Justin Gooding, J. Electrochemical "Switching" of Si(100) Modular Assemblies. *J. Am. Chem. Soc.* **2012,** *134*, 844–847.

12.   Fabre, B. Functionalization of Oxide-Free Silicon Surfaces with Redox-Active Assemblies. *Chem. Rev.* **2016,** *116*, 4808–4849.

13.   Aragonès, A. C.; Darwish, N.; Ciampi, S.; Sanz, F.; Gooding, J. J.; Diéz-Pérez, I. Single-molecule electrical contacts on silicon electrodes under ambient conditions. *Nat. Commun.* **2017,** *8*, 15056–15056.

14.   Ferrie, S.; Darwish, N.; Gooding, J. J.; Ciampi, S. Harnessing silicon facet-dependent conductivity to enhance the direct-current produced by a sliding Schottky diode triboelectric nanogenerator. *Nano Energy* **2020,** *78*, 105210.

15.   Ferrie, S.; Le Brun, A. P.; Krishnan, G.; Andersson, G. G.; Darwish, N.; Ciampi, S. Sliding silicon-based Schottky diodes: Maximizing triboelectricity with surface chemistry. *Nano Energy* **2022,** *93*, 106861.

16.   Zhang, S.; Ferrie, S.; Peiris, C. R.; Lyu, X.; Vogel, Y. B.; Darwish, N.; Ciampi, S. Common Background Signals in Voltammograms of Crystalline Silicon Electrodes are Reversible Silica–Silicon Redox Chemistry at Highly Conductive Surface Sites. *J. Am. Chem. Soc.* **2021,** *143*, 1267–1272.

17.   Zhang, J.; Ferrie, S.; Zhang, S.; Vogel, Y. B.; Peiris, C. R.; Darwish, N.; Ciampi, S. Single-Electrode Electrochemistry: Chemically Engineering Surface Adhesion and Hardness To Maximize Redox Work Extracted from Tribocharged Silicon. *ACS Appl. Nano Mater.* **2019,** *2*, 7230–7236.

18.   Zhao, Y.; Bouffier, L.; Xu, G.; Loget, G.; Sojic, N. Electrochemiluminescence with semiconductor (nano)materials. *Chem. Sci.* **2022,** *13*, 2528–255.

19.   Tan, C. S.; Hsieh, P. L.; Chen, L. J.; Huang, M. H. Silicon Wafers with Facet-Dependent Electrical Conductivity Properties. *Angew Chem. Int. Ed.* **2017,** *129*, 15541–15545.

20.   Zhang, S.; Ferrie, S.; Lyu, X.; Xia, Y.; Darwish, N.; Wang, Z.; Ciampi, S. Absence of a Relationship between Surface Conductivity and Electrochemical Rates: Redox-Active Monolayers on Si(211), Si(111), and Si(110). *J. Phys. Chem. C* **2021,** *125*, 18197–18203.

21.   Waelder, J.; Vasquez, R.; Liu, Y.; Maldonado, S. A Description of the Faradaic Current in Cyclic Voltammetry of Adsorbed Redox Species on Semiconductor Electrodes. *J. Am. Chem. Soc.* **2022,** *144*, 6410–6419.

22.   Sharov, V. A.; Alekseev, P. A.; Borodin, B. R.; Dunaevskiy, M. S.; Reznik, R. R.; Cirlin, G. E. InP/Si Heterostructure for High-Current Hybrid Triboelectric/Photovoltaic Generation. *ACS Appl. Energy Mater.* **2019,** *2*, 4395–4401.

23.   Liu, J.; Goswami, A.; Jiang, K.; Khan, F.; Kim, S.; McGee, R.; Li, Z.; Hu, Z.; Lee, J.; Thundat, T. Direct-current triboelectricity generation by a sliding Schottky nanocontact on MoS_2 multilayers. *Nat. Nanotechnol.* **2018,** *13*, 112–116.

24.   Lyu, X.; Ferrie, S.; Pivrikas, A.; MacGregor, M.; Ciampi, S. Sliding Schottky diode triboelectric nanogenerators with current output of $109A/m^2$ by molecular engineering of Si(211) surfaces. *Nano Energy* **2022**, 107658.

25.   Olson, K. P.; Mizzi, C. A.; Marks, L. D. Band Bending and Ratcheting Explain Triboelectricity in a Flexoelectric Contact Diode. *Nano Lett.* **2022,** *22*, 3914–3921.

26.   Gooding, J. J.; Ciampi, S. The molecular level modification of surfaces: From self-assembled monolayers to complex molecular assemblies. *Chem. Soc. Rev.* **2011,** *40*, 2704–2718.

27.   Linford, M. R.; Fenter, P.; Eisenberger, P. M.; Chidsey, C. E. D. Alkyl Monolayers on Silicon Prepared from 1-Alkenes and Hydrogen-Terminated Silicon. *J. Am. Chem. Soc* **1995,** *117*, 3145–3155.

28.   Ciampi, S.; Le Saux, G.; Harper, J. B.; Gooding, J. J. Optimization of Click Chemistry of Ferrocene Derivatives on Acetylene-Functionalized Silicon(100) Surfaces. *Electroanalysis* **2008,** *20*, 1513–1519.

29.   Meldal, M.; Tornøe, C. W. Cu-Catalyzed Azide−Alkyne Cycloaddition. *Chem. Rev.* **2008,** *108*, 2952–3015.

30.   Rohde, R. D.; Agnew, H. D.; Yeo, W.-S.; Bailey, R. C.; Heath, J. R. A Non-Oxidative Approach toward Chemically and Electrochemically Functionalizing Si(111). *J. Am. Chem. Soc.* **2006,** *128*, 9518–9525.

31.   Hauquier, F.; Ghilane, J.; Fabre, B.; Hapiot, P. Conducting Ferrocene Monolayers on Nonconducting Surfaces. *J. Am. Chem. Soc.* **2008,** *130*, 2748–2749.

32.   Ouyang, J. H.; Zhao, X. S.; Li, T.; Zhang, D. C. Direct measurement of the etching rates on Si (111) and silicon dioxide surfaces in 40% ammonium fluoride aqueous solution via atomic force microscopy. *Int. J. Appl. Phys.* **2003,** *93*, 4315–4320.

33.   Williams, K. R.; Muller, R. S. Etch rates for micromachining processing. *J. Microelectromech. Syst.* **1996,** *5*, 256–269.

34.   Baski, A. A.; Erwin, S. C.; Whitman, L. J. The structure of silicon surfaces from (001) to (111). *Surf. Sci.* **1997,** *392*, 69–85.

35.   Nikolov, V.; Lin, J.; Merzlyakov, M.; Hristova, K.; Searson, P. C. Electrical Measurements of Bilayer Membranes Formed by Langmuir−Blodgett Deposition on Single-Crystal Silicon. *Langmuir* **2007,** *23*, 13040–13045.

36.   Chilcott, T. C.; Wong, E. L. S.; Böcking, T.; Coster, H. G. L. Electrical characterizations of biomimetic molecular layers on gold and silicon substrates. *Physiol. Meas.* **2008,** *29*, S307–S319.

37.   Vogel, Y. B.; Zhang, L.; Darwish, N.; Gonçales, V. R.; Le Brun, A.; Gooding, J. J.; Molina, A.; Wallace, G. G.; Coote, M. L.; Gonzalez, J.; Ciampi, S. Reproducible Flaws Unveil Electrostatic Aspects of Semiconductor Electrochemistry. *Nat. Commun.* **2017,** *8*, 2066.

38.   Vogel, Y. B.; Molina, A.; Gonzalez, J.; Ciampi, S. Quantitative Analysis of Cyclic Voltammetry of Redox Monolayers Adsorbed on Semiconductors: Isolating Electrode Kinetics, Lateral Interactions, and Diode Currents. *Anal. Chem.* **2019,** *91*, 5929–5937.

39.   Gonçales, V. R.; Lian, J.; Gautam, S.; Tilley, R. D.; Gooding, J. J. Functionalized Silicon Electrodes in Electrochemistry. *Annu. Rev. Anal. Chem.* **2020,** *13*, 135–158.

40.   Choudhury, M. H.; Ciampi, S.; Yang, Y.; Tavallaie, R.; Zhu, Y.; Zarei, L.; Gonçales, V. R.; Gooding, J. J. Connecting Electrodes with Light: One Wire, Many Electrodes. *Chem. Sci.* **2015,** *6*, 6769–6776.

41.   Vogel, Y. B.; Gooding, J. J.; Ciampi, S. Light-addressable electrochemistry at semiconductor electrodes: redox imaging, mask-free lithography and spatially resolved chemical and biological sensing. *Chem. Soc. Rev.* **2019,** *48*, 3723–3739.

42.   Chidsey, C. E. D.; Bertozzi, C. R.; Putvinski, T. M.; Mujsce, A. M. Coadsorption of ferrocene-terminated and unsubstituted alkanethiols on gold: electroactive self-assembled monolayers. *J. Am. Chem. Soc.* **1990,** *112*, 4301–4306.

43.   Ciampi, S.; Choudhury, M. H.; Ahmad, S. A. B. A.; Darwish, N.; Brun, A. L.; Gooding, J. J. The impact of surface coverage on the kinetics of electron transfer through redox monolayers on a silicon electrode surface. *Electrochim. Acta* **2015,** *186*, 216–222.

44.   Gerischer, H.; Mindt, W. The mechanisms of the decomposition of semiconductors by electrochemical oxidation and reduction. *Electrochim. Acta* **1968,** *13*, 1329–1341.

45.   Allongue, P.; Kieling, V.; Gerischer, H. Etching mechanism and atomic structure of H-Si(111) surfaces prepared in NH₄F. *Electrochim. Acta* **1995,** *40*, 1353–1360

46.   Palik, E. D.; Glembocki, O. J.; Heard, I. H. Study of bias-dependent etching of Si in aqueous KOH. *J. Electrochem. Soc.* **1987,** *134*, 404–409.

47.   Chadi, D. J. Theoretical study of the atomic structure of silicon (211), (311), and (331) surfaces. *Phys. Rev., B Condens.* **1984,** *29*, 785–792.

48.   Vaziri Hassas, B.; Caliskan, H.; Guven, O.; Karakas, F.; Cinar, M.; Celik, M. S. Effect of roughness and shape factor on flotation characteristics of glass beads. *Colloids Surf. A Physicochem. Eng. Asp.* **2016,** *492*, 88–99.

49.   Thong, J. T. L.; Choi, W. K.; Chong, C. W. TMAH etching of silicon and the interaction of etching parameters. *Sens. Actuator A Phys.* **1997,** *63*, 243–249.

50.   Zhang, S.; Lyu, X.; Hurtado Torres, C.; Darwish, N.; Ciampi, S. Non-Ideal Cyclic Voltammetry of Redox Monolayers on Silicon Electrodes: Peak Splitting is Caused by Heterogeneous Photocurrents and Not by Molecular Disorder. *Langmuir* **2022,** *38*, 743–750.

51.   Rudnev, A. V.; Yoshida, K.; Wandlowski, T. Electrochemical characterization of self-assembled ferrocene-terminated alkanethiol monolayers on low-index gold single crystal electrodes. *Electrochim. Acta* **2013,** *87*, 770–778.

52.   Madou, M. J.; Loo, B. H.; Frese, K. W.; Morrison, S. R. Bulk and surface characterization of the silicon electrode. *Surf. Sci.* **1981,** *108*, 135–152.

53.   Uritsky, V. X. Role of Electron / Hole Processes in the Initial Stage of Silicon Anodization. *Mater. Sci. Forum* **1995,** *185-188*, 115–118.

54.   Gonzalez, J.; Sequi, J.-A. Analysis of the Electrochemical Response of Surface–confined Bidirectional Molecular Electrocatalysts in the Presence of Intermolecular Interactions. *ChemCatChem* **2021,** *13*, 747–762.

55.   Gonzalez, J.; Sequí-Castellano, J. A. Electrochemical determination of kinetic parameters of surface confined redox probes in presence of intermolecular interactions by means of Cyclic Voltammetry. Application to TEMPO monolayers in gold and platinum electrodes. *Electrochim. Acta* **2021,** *365*, 137331.

56.   Zhang, L.; Vogel, Y. B.; Noble, B. B.; Gonçales, V. R.; Darwish, N.; Brun, A. L.; Gooding, J. J.; Wallace, G. G.; Coote, M. L.; Ciampi, S. TEMPO Monolayers on Si(100) Electrodes: Electrostatic Effects by the Electrolyte and Semiconductor Space-Charge on the Electroactivity of a Persistent Radical. *J. Am. Chem. Soc.* **2016,** *138*, 9611–9619.

57.   Cicero, R. L.; Linford, M. R.; Chidsey, C. E. D. Photoreactivity of Unsaturated Compounds with Hydrogen-Terminated Silicon(111). *Langmuir* **2000,** *16*, 5688–5695.

58.   Bashouti, M. Y.; Paska, Y.; Puniredd, S. R.; Stelzner, T.; Christiansen, S.; Haick, H. Silicon nanowires terminated with methyl functionalities exhibit stronger Si–C bonds than equivalent 2D surfaces. *Phys. Chem. Chem. Phys.* **2009,** *11*, 3845–3848

59.   Wallart, X.; Henry de Villeneuve, C.; Allongue, P. Truly Quantitative XPS Characterization of Organic Monolayers on Silicon: Study of Alkyl and Alkoxy Monolayers on H−Si(111). *J. Am. Chem. Soc.* **2005,** *127*, 7871–7878.

60.   Scheres, L.; Arafat, A.; Zuilhof, H. Self-Assembly of High-Quality Covalently Bound Organic Monolayers onto Silicon. *Langmuir* **2007,** *23*, 8343–8346.

61.   Cerofolini, G. F.; Galati, C.; Renna, L. Accounting for anomalous oxidation states of silicon at the Si/SiO$_2$ interface. *Surf. Interface Anal.* **2002,** *33*, 583–590.

62.   Ito, E.; Oji, H.; Araki, T.; Oichi, K.; Ishii, H.; Ouchi, Y.; Ohta, T.; Kosugi, N.; Maruyama, Y.; Naito, T.; Inabe, T.; Seki, K. Soft X-ray Absorption and X-ray Photoelectron Spectroscopic Study of Tautomerism in Intramolecular Hydrogen Bonds of N-Salicylideneaniline Derivatives. *J. Am. Chem. Soc.* **1997,** *119*, 6336–6344.

63.   Böcking, T.; James, M.; Coster, H. G. L.; Chilcott, T. C.; Barrow, K. D. Structural Characterization of Organic Multilayers on Silicon(111) Formed by Immobilization of Molecular Films on Functionalized Si−C Linked Monolayers. *Langmuir* **2004,** *20*, 9227–9235.

64.   Sieval, A. B.; Demirel, A. L.; Nissink, J. W. M.; Linford, M. R.; van der Maas, J. H.; de Jeu, W. H.; Zuilhof, H.; Sudhölter, E. J. R. Highly Stable Si−C Linked Functionalized Monolayers on the Silicon (100) Surface. *Langmuir* **1998,** *14*, 1759–1768.

65.   Li, T.; Dief, E. M.; Lyu, X.; Rahpeima, S.; Ciampi, S.; Darwish, N. Nanoscale Silicon Oxide Reduces Electron Transfer Kinetics of Surface-Bound Ferrocene Monolayers on Silicon. *J. Phys. Chem. C.* **2021,** *125*, 27763–27770.

66.   Ren, L.; Yu, A.; Wang, W.; Guo, D.; Jia, M.; Guo, P.; Zhang, Y.; Wang, Z. L.; Zhai, J. p-n Junction Based Direct-Current Triboelectric Nanogenerator by Conjunction of Tribovoltaic Effect and Photovoltaic Effect. *Nano Lett.* **2021,** *21*, 10099–10106.

67.   Zheng, Q.; Peng, M.; Liu, Z.; Li, S.; Han, R.; Ouyang, H.; Fan, Y.; Pan, C.; Hu, W.; Zhai, J.; Li, Z.; Wang, Z. L. Dynamic real-time imaging of living cell traction force by piezo-phototronic light nano-antenna array. *Sci. Adv. 7*, eabe7738.

68.   Peng, M.; Liu, Y.; Yu, A.; Zhang, Y.; Liu, C.; Liu, J.; Wu, W.; Zhang, K.; Shi, X.; Kou, J.; Zhai, J.; Wang, Z. L. Flexible Self-Powered GaN Ultraviolet Photoswitch with Piezo-Phototronic Effect Enhanced On/Off Ratio. *ACS Nano* **2016,** *10*, 1572–1579.

69.   Miller, J. N. a., *Statistics and chemometrics for analytical chemistry / James N. Miller, Jane C. Miller, Robert D. Miller*. Seventh edition. ed.; Harlow, United Kingdom : Pearson Education Limited: 2018.

70.   Laviron, E. A.C. Polarography and faradaic impedance of strongly adsorbed electroactive species: Part III. Theoretical complex plane analysis for a surface redox reaction. *J. Electroanal. Chem. Interf. Electrochem.* **1979,** *105*, 35–42.

Triboelectric nanogenerators on Si(211)